

Characterization of concrete failure behavior: a comprehensive experimental database for the calibration and validation of concrete models

Roman Wendner · Jan Vorel · Jovanca Smith ·
Christian G. Hoover · Zdeněk P. Bažant ·
Gianluca Cusatis

Received: 17 March 2014 / Accepted: 16 September 2014 / Published online: 30 September 2014
© RILEM 2014

Abstract Concrete is undoubtedly the most important and widely used construction material of the late twentieth century. Yet, mathematical models that can accurately capture the particular material behavior under all loading conditions of significance are scarce at best. Although concepts and suitable models have existed for quite a while, their practical significance is low due to the limited attention to calibration and validation requirements and the scarcity of robust, transparent and comprehensive methods to perform such tasks. In addition, issues such as computational cost, difficulties associated with calculating the response of highly nonlinear systems, and, most importantly, lack of comprehensive experimental data sets

have hampered progress in this area. This paper attempts to promote the use of advanced concrete models by (a) providing an overview of required tests and data preparation techniques; and (b) making a comprehensive set of concrete test data, cast from the same batch, available for model development, calibration, and validation. Data included in the database '<http://www.baunat.boku.ac.at/cd-labor/downloads/versuchsdaten>' comprise flexure tests of four sizes, direct tension tests, confined and unconfined compression tests, Brazilian splitting tests of five sizes, and loading and unloading data. For all specimen sets the nominal stress–strain curves and crack patterns are provided.

Keywords 3-Point bending · Brazilian splitting · Size effect · Cohesive fracture · Softening · Single notch tension

R. Wendner · J. Vorel
Christian Doppler Laboratory, University of Natural
Resources and Life Sciences Vienna, Peter-Jordanstr. 82,
1190 Vienna, Austria

J. Vorel
Czech Technical University in Prague, Thakurova 7,
16629 Prague, Czech Republic

J. Smith · Z. P. Bažant · G. Cusatis (✉)
Technological Institute, Northwestern University, 2145
Sheridan Road, Evanston, IL 60208, USA
e-mail: g-cusatis@northwestern.edu

C. G. Hoover
Massachusetts Institute of Technology, 77 Massachusetts
Avenue, Cambridge, MA 02139, USA

1 Introduction

Rapid progress in concrete technology in recent years has led to the development of many new construction materials with novel properties. These are, among others, ultra-high performance concretes (UHPC) with strengths of up to 200 MPa [1], self consolidating concretes (SCC) with improved rheology [2], fiber reinforced concretes (FRC) characterized by significantly increased ductility [3, 4], and engineered

cementitious composites (ECC) with superior impact resistance [5].

This development provides many opportunities for the construction industry, associated with as many challenges. The main obstruction for a wide-spread application of these novel materials is a significant lack of experience. Traditionally, design codes were developed based on large experimental investigations and multi-decade practical experience. Thus, safe design rules could be ensured that are typically characterized by sufficiently conservative assumptions. This approach, however, can no longer satisfy the requirements of modern construction industry and it is increasingly less sustainable from the economic point of view. The only feasible solution is supplementing experiments with analytical predictions based on accurate, reliable, and validated models. Simulations can provide the means for virtual testing of structural capacity, performance, and, ultimately, also life-time, if structural analysis is coupled with multi-physics and deterioration modeling.

The main characteristics of the tensile behavior of concrete and other quasi-brittle materials are cracking and strain softening—a loss of carrying capacity for increasing deformation. Such behavior is typically described by non-linear fracture mechanics and suitable strain softening laws, characterized by the total fracture energy G_F or, equivalently, by Hillerborg's characteristic length [6, 7], $l_{ch} = EG_F/f_t'^2$ (E = Young's modulus; f_t' = tensile strength) which was derived based on Irwin's approximation for the size of the plastic zone in ductile materials [8, 9]. The most important effect of strain softening is the dependence of structural strength on structural size [8]—any mathematical model for concrete that has any value must be able to simulate size-effect. Concrete behavior in compression is even more complicated: under low or no confinement the compressive behavior features brittleness and strain-softening; for increasing confinement, however, the behavior transitions from strain-softening to strain-hardening and it is characterized by significant ductility. Under sufficient lateral confinement concrete can reach strains over 100 % without the loss of load carrying capacity and visible damage [10–14].

Over the years many constitutive models have been developed to describe the behavior of concrete. They

utilize the concepts of plasticity [15, 16], damage mechanics [17, 18] or fracture mechanics [8, 18] and they are typically formulated in tensorial form by using the classical framework of continuum mechanics. Continuum constitutive equations can also be formulated in vectorial form through the microplane theory [19, 20], which has a number of advantages over tensorial formulations. Microplane models do not need to be formulated as functions of macroscopic stress and strain tensor invariants [21] and the principle of frame indifference, however, is satisfied by using microplanes that sample (without bias) all possible orientations in the three-dimensional space. The constitutive laws specified on the microplanes are activated by employing either the kinematic or the static constraints. The former defines the microplane strains as projections of the macroscopic strain tensor whereas the latter defines the microplane stresses as projections of the macroscopic stress tensor. Kinematically constrained formulations can be used with microplane constitutive laws exhibiting softening and for this reasons they have been adopted for quasi-brittle materials [22] such as concrete [23–25], even at early age [26], rocks [21], and composite laminates [27, 28].

For continuum formulations, objectivity of the solution and independence of the numerical solution upon the finite element discretization have to be either inherent to the constitutive model, as for example in the case of high order [29] and nonlocal [30, 31] models, or must be imposed using regularization techniques such as the crack band approach [8, 32]. Methods that do not suffer from mesh sensitivity are also the ones accounting for strain softening through the insertion of cohesive discrete cracks [6, 33–36].

Another class of models often used to simulate quasi-brittle materials is based on lattice or particle formulations in which materials are discretized “a priori” according to an idealization of their internal structure. Particle size and size of the contact area among particles, for particle models, as well as lattice spacing and cross sectional area, for lattice models, equip these type of formulations with inherent characteristic lengths and they have the intrinsic ability of simulating the geometrical features of material internal structure. This allows the accurate simulation of damage initiation and crack propagation at various length scales at the cost, however, of increased computational costs.



Earlier attempts to formulate particle and lattice models for fracture are reported in [37–43] while the most recent developments were published in a Cement Concrete Composites special issue [44]. A comprehensive discrete formulation for concrete was recently proposed by Cusatis and coworkers [45–50] who formulated the so-called Lattice Discrete Particle Model (LDPM). LDPM was calibrated, and validated against a large variety of loading conditions in both quasi-static and dynamic loading conditions and it was demonstrated to possess superior predictive capability.

As evident from the short review presented above, many different concrete material models are available in the literature. However, the challenge that still remains is selecting the model that is most suitable for a given application, and obtaining the required input parameters. These can either have direct physical meaning or be solely model parameters that have to be inversely identified. However, in all cases sufficient experimental data are required to uniquely determine and finally validate the model parameters. This entails the availability of data of all required test types with sufficient number of samples to yield statistically meaningful results. Required tests include, but are not limited to, uniaxial compression, confined compression or triaxial tests, and direct or indirect tension tests. From these strength and modulus information as well as hardening parameters can be derived. Due to the brittle nature of concrete indirect tension tests such as 3-point-bending or splitting are generally preferred. In order to ensure unique softening parameters, softening post-peak data for at least two sizes [51] or alternatively two different types of tests, should be obtained. For FRC bond properties and fiber characteristics are to be determined additionally [52]. Further tests are required if predictions under high loading rates, or extreme environmental conditions have to be carried out. While for established models the predictive capabilities can be assumed to be satisfactory after calibration, new models also need to be validated. This step includes a subdivision of tests and specimens into sub-populations for calibration and prediction, where a random subset (typically 1/2 to 2/3) is allocated to calibration and the rest (ideally encompassing tests of all types) are used for prediction and validation.

This paper focuses on the discussion of relevant tests for the calibration and validation of concrete models. In particular, a comprehensive set of tests

including uniaxial compression, confined compression and size-effect tests in 3-point bending and splitting is presented. All specimen were cast from the same batch and most were tested at an age of around 400 days with the exception of standard 28-day compressive strength tests and a few additional tests that were carried out at 950 days. This practice ensured that the change of material properties during the period of testing was negligible. The raw data obtained in more than 257 tests was post-processed to provide statistical indicators for material properties and mean response curves for all types of tests including post-peak softening. The complete collection of pre-processed response curves as well as the raw data are freely available at <http://www.baunat.boku.ac.at/cd-labor/downloads/versuchsdaten/>.

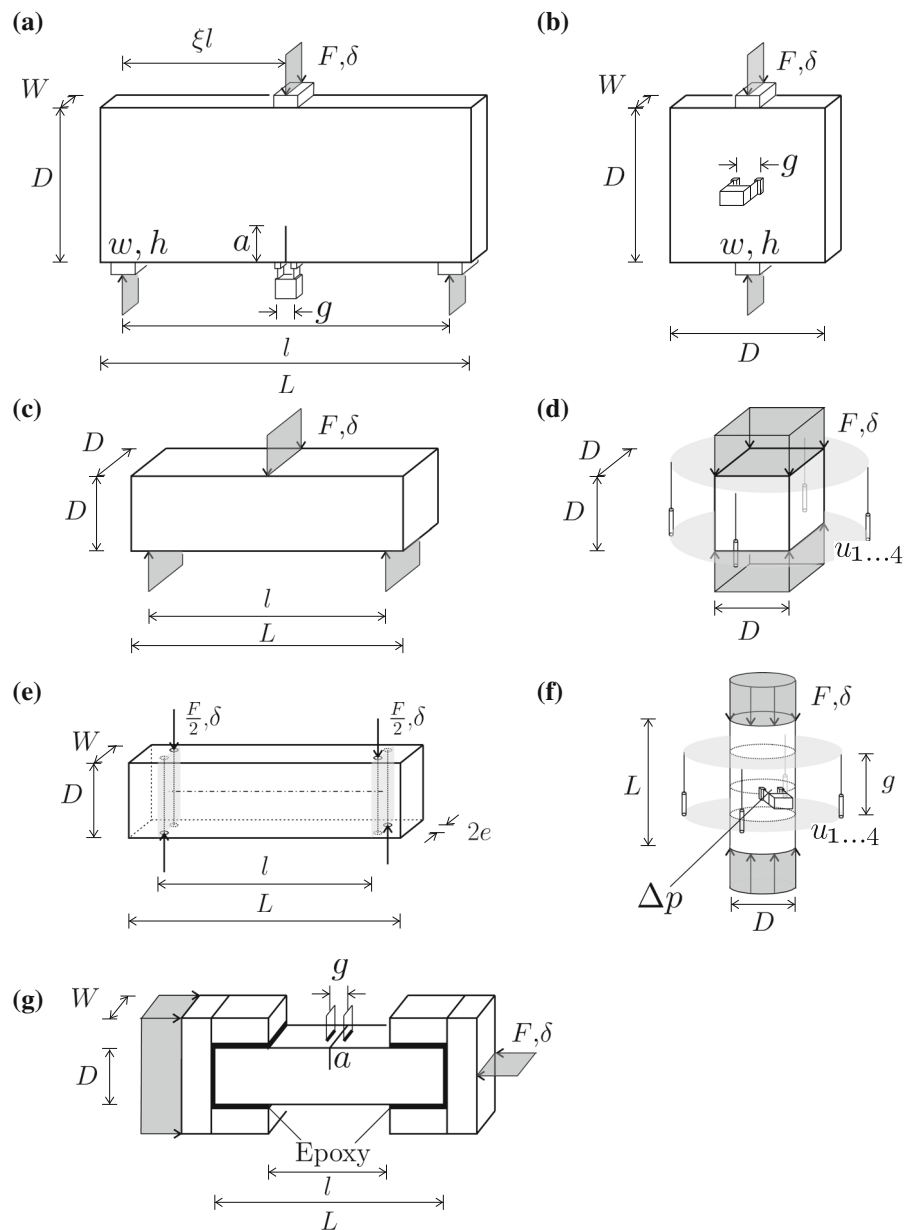
2 Scope of experimental investigation

The scientific literature contains an abundance of experimental data covering different phenomena and mechanisms. However, the number of publications reporting response curves for uniaxial compression, confined compression, direct and indirect tension of the same concrete are very limited, and basically none simultaneously provide post-peak response for various sizes.

The present investigation represents an extension of a size-effect investigation in 3-point bending conducted by Hoover et al. [53] during which a total of 164 concrete specimens were cast in one batch (see Sect. 2.1) in early 2011 and tested in 2012. A similar investigation dedicated to the fracture properties of self-consolidating concretes of various compositions is presented in Beygi et al. [54]. Afterwards, additional 105 specimens were cut from the remaining shards in order to supplement, among others, confined compression tests, Brazilian splitting tests, direct tension tests, and hysteretic loading-unloading tests. For all fracture tests of the initial and extended investigation the crack pattern was documented photographically and digitized by photogrammetric means. In detail, response curves for the following tests are available:

- 128 three-point bending tests of 400 day old geometrically scaled un-reinforced concrete beams of four sizes with a size range of 1:12.5

Fig. 1 Specimen geometry: **a** three point bending tests, geometrically scaled in four sizes, **b** Brazilian splitting tests, geometrically scaled in five sizes, **c** ASTM modulus of rupture tests [55], **d** unconfined compression of cubes of two sizes, **e** torsion tests, **f** unconfined cylinder tests of two sizes, and **g** single notched tension tests



including un-notched specimens and beams with relative notch depths of $\alpha = a/D = 0.30, 0.15, 0.075, 0.025$, see Fig. 1a.

- 12 centrally and eccentrically loaded 466 day old 3-point bending specimens of depth size $D = 93$ mm according to Fig. 1a, with and without unloading cycles in the softening regime.
- 40 Brazilian splitting tests, of roughly 475 day old prismatic specimens of 5 sizes with a size range of 1:16.7, see Fig. 1b.

- 12 standard ASTM modulus of rupture tests [55] at 31 days and 400 days, see Fig. 1c.
- 24 uniaxial compression tests of 75×150 mm ($3'' \times 6''$) cylinders at 31 days and 400 days, see Fig. 1f.
- 22 uniaxial compression tests of approximately 470 day old cubes of side lengths $D = 40$ and $D = 150$ mm, loaded partly monotonically and partly with several loading-unloading cycles in the softening regime, see Fig. 1d.

- 6 uniaxial compression tests of approximately 950 day old cubes of side length $D = 40$ mm
- 6 uniaxial tension tests of approximately 950 day old prisms, see Fig. 1g
- 4 confined compression tests of 560 day old cored cylinders of diameter $D = 50$ mm and length $L = 40$ mm including 4 unconfined uniaxial compression tests of cored companion specimens.
- 11 torsion tests of prisms with constant thickness $W = 40$ mm and depths $D = 40, 60, 80$ mm according to Fig. 1e.

Full or partial post-peak data are available for all tests except the ASTM modulus of rupture tests and the confined compression tests. Due to the multitude of sizes and specimen geometries all plots are presented in terms of nominal stress σ_N and nominal strain ϵ_N , the definition of which is given in the respective subsections of Sect. 3.

2.1 Mix properties and curing

All 164 specimens of the initial investigation (128 beams, 12 ASTM beams, 24 cylinders) were cast in one batch of ready-mixed concrete with a specified compressive strength $f'_c = 31$ MPa. On top of 354.8 kg/m^3 cement (CEM I, ordinary portland cement) the mix design includes 59.9 kg/m^3 fly ash, resulting in a water-cement ratio $w/c = 0.41$, and a water-binder ratio $w/b = 0.35$, respectively. The aggregate to binder ratio $a/b = 4.43$ is achieved through the addition of 863 sand and $1,015 \text{ kg/m}^3$ coarse aggregate (pea gravel, consisting of glacial outwash deposits from McHenry, Illinois) with a maximum aggregate diameter of 10 mm. The mix further contains 0.78 kg/m^3 of water reducer, 2.08 kg/m^3 superplasticizer and 0.56 kg/m^3 retarder. The addition of these admixtures was required to guarantee a consistent 150 mm of slump throughout the 3 h casting.

The 128 beams of the original size effect investigation were cast horizontally in molds with constant depth of $W = 40$ mm. Immediately after casting the beams and cylinders were covered with plastic and remained untouched for 36 h after which they were demolded and relocated to a fog-curing room. There they were stored under ambient temperature conditions (around 23°C) and at roughly 98 % relative humidity until testing. Immediately after testing the

Table 1 Material properties extracted from cylinder tests and ASTM modulus of rupture tests

Material property		Unit	Mean	CoV (%)
Compressive cylinder strength	$f_{cy,75}(31)$	MPa	46.5	3.2
Compressive cylinder strength	$f_{cy,75}(400)$	MPa	55.6	3.7
Compressive cube strength	$f_{cu,40}(470)$	MPa	56.6	9.5
Compressive cube strength	$f_{cu,150}(470)$	MPa	57.1	5.5
Compressive cube strength	$f_{cu,40}(950)$	MPa	61.2	8.2
ASTM modulus of rupture	$f_r(31)$	MPa	6.7	5.2
ASTM modulus of rupture	$f_r(400)$	MPa	8.3	3.6
Modulus of elasticity, 75 mm cyl	$E_{cy,75}(31)$	GPa	27.74	6.2
Modulus of elasticity, 75 mm cyl	$E_{cy,75}(400)$	GPa	34.38	3.9
Modulus of elasticity, $D = 40$ mm	$E_{r,40}(400)$	GPa	35.70	7.0
Modulus of elasticity, $D = 93$ mm	$E_{r,93}(400)$	GPa	41.29	6.8
Modulus of elasticity, $D = 215$ mm	$E_{r,215}(400)$	GPa	43.68	9.4
Modulus of elasticity, $D = 500$ mm	$E_{r,500}(400)$	GPa	43.66	12.7
Modulus of elasticity, inverse	$E_{inv}(400)$	GPa	37.94	
Poisson ratio	ν	–	0.172	10.0

shards of the bending test specimens were again stored in the fog-curing room. Special attention was placed on minimizing the transfer time between testing and storage to avoid uncontrolled shrinkage cracking.

The additional investigations were performed on specimens that were cut or cored out of the shards of the original investigation. Special attention was placed on avoiding areas of high stress concentration (support points) and pre-damaged areas including e.g. the original fracture process zone (FPZ). The additional specimens as well as the notches were cut with a diamond coated band saw with water cooling. In each case the exposure time to unsaturated humidity conditions was limited to a minimum.

2.2 Overview of material properties

The basic concrete properties have been extracted from various tests performed at different ages. For convenience a summary is provided in Table 1, see also Hoover et al. [53]. In addition to the experimental results the inversely obtained 400-day modulus, extracted from 93-mm 3-point bending tests, is presented. Relevant fracture parameters are given in Table 3. Where possible the inherent scatter of the experiments is quantified by the coefficient of variation $\text{CoV} = \text{std}/\text{mean}$. The high carefulness in casting, specimen preparation, and testing was rewarded by a remarkably low experimental scatter with coefficient variation less than 10 % and a minimum of statistical outliers. Only two of the early age compression cylinders and one of the beams failed the Grubb's test for outliers [56, 57], assuming a significance level of $\alpha = 0.05$. The respective specimens were excluded from all further analyses. Compressive strength was determined based on 75×150 mm cylinders, 40 and 150 mm cubes. The reported Poisson's ratio was determined based on the circumferential expansion of standard cylinders in compression [53].

The strength and modulus development can be predicted by Eq. (1) according to the fib Model code 2010 with parameter $s = 0.25$ for R-type cement [58] and a reference age $t_{\text{ref}} = 28$ days.

$$\begin{aligned} f(t) &= f_{28} \beta_{\text{fib}}(t), & E(t) &= E_{28} \sqrt{\beta_{\text{fib}}(t)}, \\ \beta_{\text{fib}}(t) &= e^{s(1-\sqrt{t_{\text{ref}}/t})} \end{aligned} \quad (1)$$

The equivalent ACI formulation is given by Eq. (2) with $a = 4.0$ and $b = 0.85$ for Type-I cement [59].

$$\begin{aligned} f(t) &= f_{28} \beta_{\text{ACI}}(t), & E(t) &= E_{28} \sqrt{\beta_{\text{ACI}}(t)}, \\ \beta_{\text{ACI}}(t) &= \frac{t}{a + bt} \end{aligned} \quad (2)$$

While the model code prediction for the strength development is very good and the ACI prediction is fair, both formulations fail to predict the modulus development. In Table 2 the extracted 28-day strength and modulus values are given including the 95 % confidence bounds and the root mean square error (RMSE) of the fit. In order to fit the modulus development data the square-root dependency on strength would have to be replaced by the

Table 2 Strength and modulus development: quality of fit expressed in terms of RMSE

Parameter	Model	Value	Unit	RMSE
$f_{\text{cyl},75}(28)$	fib	46.1 [45.6, 46.6]	MPa	0.184
$f_{\text{cyl},75}(28)$	ACI	46.8 [43.4, 50.3]	MPa	1.243
$f_t(28)$	fib	6.8 [6.4, 7.2]	MPa	0.158
$f_t(28)$	ACI	6.9 [6.0, 7.8]	MPa	0.314
$E_{\text{cyl},75}(28)$	fib	29.63 [23.88, 35.37]	GPa	1.988
$E_{\text{cyl},75}(28)$	ACI	29.81 [23.08, 36.54]	GPa	2.313
$E_{\text{cyl},75}(28)$	fib ^a	27.31	GPa	–
$E_{\text{cyl},75}(28)$	ACI ^a	26.78	GPa	–

^a The models with fitted exponents)

fitted exponents 5/3 for the ACI model (ACI*, [59]), and 5/4 respectively for the fib model (fib*, [58]).

The Young's modulus can be predicted from compressive strength utilizing either the ACI (Eq. (3)) or the fib (Eq. (4)) formulation. The parameters E_0 and α_E in the latter are dependent on aggregate type. The default values for quartzite are $E_0 = 21.50$ GPa and $\alpha_E = 1.0$. The ACI prediction for the 28-day Young's Modulus yields 32.39 GPa and overestimates the experimentally identified value of 29.81 GPa. The fib equation gives an initial tangent stiffness of 35.78 GPa which corresponds to a reduced modulus

$E_c = (0.8 + 0.2f_{\text{cm}}/88 \text{ MPa})E_{\text{ci}} = 32.38$ GPa, a value almost identical with the ACI prediction.

$$E_{28,\text{ACI}} = 4734 \sqrt{f_{28}} \quad (3)$$

$$E_{28,\text{ci},\text{fib}} = E_0 \alpha_E (f_{28}/10 \text{ MPa})^{1/3} \quad (4)$$

Hoover et al. [60] studied the size-effect [8] in 3-point-bending based on the presented data-set. The values he obtained for the initial fracture energy G_F by inverse fitting of Bažant's Size Effect Law [8] as well as for the total fracture energy G_F based on the work of fracture method with bilinear softening stress-separation curve [7, 61, 62] are given in Table 3. As expected, the initial fracture energy accounts for approximately 50 % of the total fracture energy. The fib prediction of $G_F = 73f_{\text{cm}}^{0.18} = 150.5$ J/m² (with f_{cm} in MPa) overestimates the experimentally obtained value by 50 %. Further comparisons with empirical equations can be found in [60].



Table 3 Fracture parameters according to Hoover et al. [60]

Material Property		Unit	Mean	CoV (%)
Fitting of Type 2 SEL, $\alpha = 0.30$				
Initial fracture energy	G_f	N/m	51.87	–
Characteristic length	c_f	m	23.88	–
Fitting of Type 2 SEL, $\alpha = 0.15$				
Initial fracture energy	G_f	N/m	49.78	–
Characteristic length	c_f	m	20.99	–
Work of fracture method, $\alpha = 0.30$				
Total fracture energy	G_F	N/m	96.94	16.9
Work of fracture method, $\alpha = 0.15$				
Total fracture energy	G_F	N/m	111.1	20.7

3 Detailed description of tests

3.1 Test setup, instrumentation and control

All the tests were performed on servo-hydraulic closed-loop load frames with capacities of 4.5 MN, 980 kN, and 89 kN respectively. Uniaxial compression and confined compression tests were carried out in the 4.5 MN load frame. For the ASTM standard modulus of rupture tests [55], the notched and unnotched 3-point bending tests, as well as splitting tests of specimens with size $D = 215$ mm and $D = 500$ mm the 1,000 kN load frame was used. All the remaining specimens were tested in the 90 kN load frame. In general a loading time of 5 min to peak, based on preliminary predictions, was attempted.

During specimen preparation all relevant dimensions were rigorously recorded. The initial condition of each specimens as well as the crack pattern of the failed specimens were documented with pictures, the latter of which served for the crack path digitization reported in Sect. 3.6. Piston movement (stroke), force, and loading time are available with a sampling frequency of 1 Hz for all specimens. Additionally, the test specific quantities load-point displacement, circumferential expansion, axial shortening, and crack mouth opening displacement (CMOD) were recorded. Further information can be found in the test specific sections 3.4–3.8.

3.2 Test control and stability

A particular challenge in the testing of quasi-brittle materials is associated with obtaining post-peak

softening response for different types of tests and, ideally, various sizes. This information is quintessential for calibrating the model parameters which control softening in tension, shear-tension, or compression under low confinement. The ability to control a specimen in the softening regime is a stability problem, which, in its most general form, can be described by an energetic stability condition formulated in terms of the second variation of the potential energy $\delta^2\Pi > 0$ [17]. It can be shown that under displacement control the equilibrium path remains stable as long as no point with vertical slope is reached. This limit state is called “snap-down” and represents the transition to a “snap-back” instability which is characterized by an equilibrium path with global energy release. In the softening regime parts of the system (load frame as well as specimen) are elastically unloading, releasing energy. Depending on the experiment the contributions of both vary and in many cases they are negligible. While the energy release within the specimen is out of the control of the experimenter (and can also be observed in numerical simulations), the energy released by the unloading load frame can be controlled through its compliance.

The practical problem of a specimen with elastic stiffness K_{el} in a load-frame with stiffness K_m is equivalent to a serial system with total current tangential stiffness $K(u) = \{1/K_m + 1/[K_{el} - \Delta K(u)]\}^{-1}$, where $[K_{el} - \Delta K(u)] =$ true tangential specimen stiffness, and $\Delta K(u) =$ total stiffness change due to softening. A stable test in displacement control in the softening regime is possible if $\Delta u > 0$, equivalent to $1/K(u) \neq 0$ along the entire equilibrium path. Consequently, a minimum machine stiffness is required for stable tests, given by the condition $K_m > K_{el} - \Delta K(u)$.

In Fig. 2a the problem of stable displacement control is illustrated utilizing experimental data for a 93 mm beam with a relative notch depth $\alpha = 0.15$ according to Fig. 1a. The observed mean load–displacement curve (thick solid line), plotted in terms of nominal strain ϵ_N and stress σ_N , see Sect. 3.6, clearly exhibits a significant snapback. Stable control in neither force nor displacement control (stroke) is possible. However, any observed response from a stably controlled test (e.g. using CMOD control, see below) can be corrected to account for the machine compliance and to recover the proper elastic stiffness

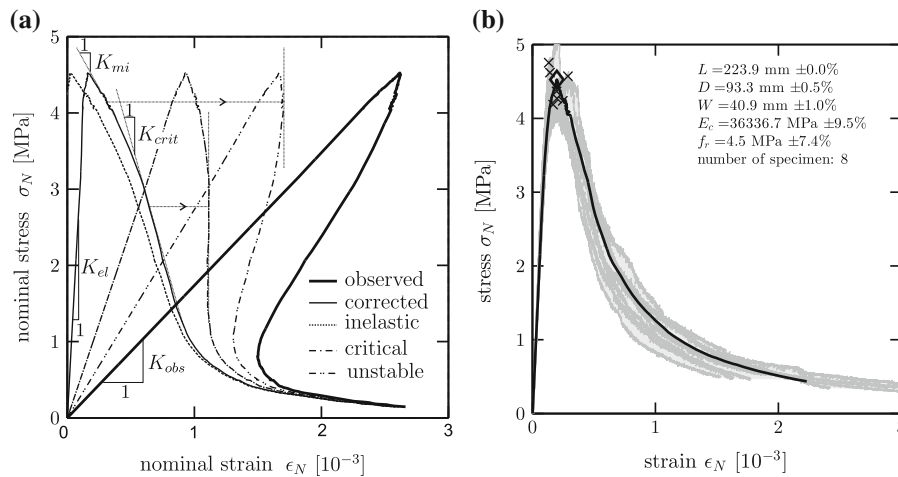


Fig. 2 Stability of fracture tests: **a** observed, inelastic, corrected, and critical response for 93 mm beams and $\alpha = 0.15$, **b** observed stable load versus opening curves for 93 mm beams and $\alpha = 0.15$

K_{el} . The results are the inelastic strain component ϵ_{inel} (thin dotted line) and the unbiased specimen response ϵ_{spec} (thin solid line).

$$\epsilon_{inel} = \epsilon_{obs} - \sigma(1/K_{obs}) \quad (5)$$

$$\epsilon_{spec} = \epsilon_{obs} + \sigma(1/K_{el} - 1/K_{obs}) \quad (6)$$

In the example discussed above the specimen itself exhibits no snapback and an entirely stable test in displacement control would have been possible for a machine stiffness $K_m > K_{crit} = 5.9$ GPa, where K_{crit} is the slope of the steepest section of the softening response. The critical state of softer load frames with a stiffness K_{mi} less than K_{crit} may be found by drawing a tangent of downward slope K_{mi} as sketched in Fig. 2a for $K_{mi} = 3$ GPa. Approximate machine compliances for the used load frames are given in Hoover et al. [53].

Practically speaking, a stable post-peak test is possible if a monotonously increasing continuous quantity for control can be found. Up to this point, displacement control based on piston movement or load-point displacement was assumed. However, many more displacement measures exist which exhibit the desired properties. True CMOD control in fracture tests or circumferential expansion control in unconfined compression tests are unconditionally stable. Crack initiation specimens such as un-notched beams or splitting prisms can be controlled by average strain, or, in general, by relative displacements between given points on a specimen that include the forming macro-crack. In the latter case the appropriate gauge

length is determined by two contradictory requirements. The amount of elastically unloading material within the monitored distance has to be minimized while the gauge length must be large enough to contain the forming crack with high likelihood.

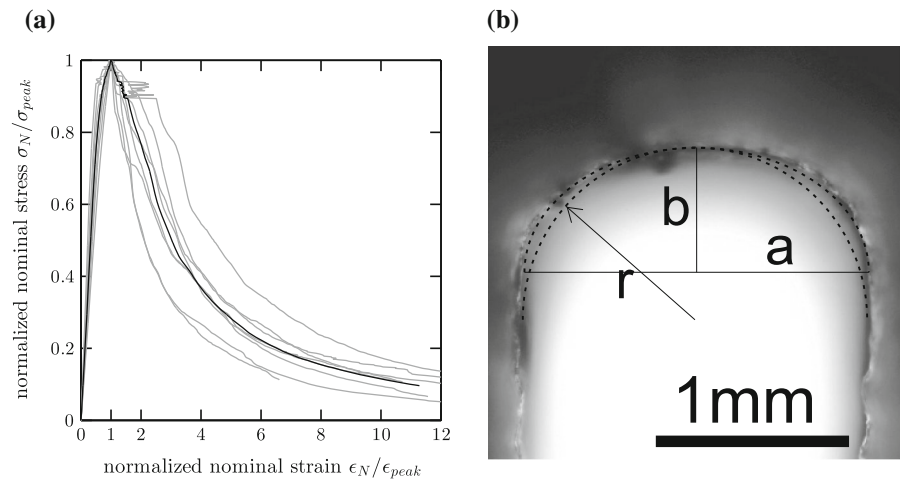
The success of fracture tests ultimately depends on the proper selection of specimen geometry, test setup, sensor instrumentation, and control mode. Thus, during the development of experimental campaigns compliance tests of the load frame, fixtures, and preliminary simulations of the specimens to determine a stable mode of control are highly advised.

3.3 Data preparation and analysis

All presented data are processed automatically, thus ensuring unbiased and objective results. The actual pre-processing is limited to determining the statistics of the specimen dimensions, the automatic removal of pre-test and post-test data and the application of a low-pass butterworth filter of order 12 with a normalized cut-off frequency of 0.10 to remove random high frequency noise.

Initial setting in load displacement diagrams is removed by linear extrapolation of the fully elastic part of the loading branch and subsequent shifting by the respective displacement intercept. The linear region is assumed to occur in the range $(0.50 - 0.90)\sigma_{peak}$ for beams, $(0.25 - 0.90)\sigma_{peak}$ for compression specimens, and $(0.60 - 0.90)\sigma_{peak}$ for splitting specimens. For the latter this range is particularly

Fig. 3 3-Point bending: **a** normalized load-CMOD curves and average response curve by the example of 3-point bending tests with $D = 93$ mm and $\alpha = 0.15$, **b** microscopic image of cut notch tip



small due to the high compliance of the used wooden support strips.

For convenience and readability of the figures the results of the individual specimen families are reported in terms of a mean response curve and envelope only. The full set of test curves is available electronically. The mean response curve is obtained by separately averaging the pre-peak and post-peak branches of the normalized curves. Each individual curve is scaled by the inverse of its peak stress σ_{peak} and peak strain ϵ_{peak} such that all peaks coincide with coordinates (1, 1). The normalized mean response curve is transformed back to match the mean nominal stress and mean nominal strain of the group of curves. Due to the possibility of snap-back strains are averaged at given stress. Figure 3 shows the normalized individual load-CMOD curves and the obtained normalized mean response curve for a 3-point bending test with depth $D = 93$ mm and non-dimensional notch depth $\alpha = 0.15$. The small variability in elastic stiffness and high similarity of the curves in the post-peak regime is illustrated.

The stroke measurements, which are the basis for some of the load displacement diagrams, obviously include contributions from the compliant load frame and fixtures. Only on-specimen deformation measurements are not distorted and can serve for the determination of the true elastic modulus. For model calibration and validation the elastic response obtained from global deformation measurements has to be corrected. Assuming that the recorded response can be decomposed in superposed inelastic and linear

elastic strain contributions, Eq. (6) is applicable for the data correction. Note that, in order to preserve the scatter in the elastic regime, K_{obs} is set equal to the elastic loading slope of the mean response for all specimens of the family.

3.4 Unconfined compression

The most traditional tests to characterize concrete are unconfined compression tests, typically performed on cylinders or cubes. The Eurocode [63, 64] allows testing both cubes of 150 mm side length and cylinders with 150 mm diameter and 300 mm height. The derived cylinder strength f_{cyl} and cube strength f_{cu} are used to specify concrete with the typical label ' Cf_{cyl}/f_{cu} '. Historically, 200 mm cubes have been used in some countries which might be of significance for the analysis of historic buildings. The standard compression tests according to ASTM C39 [65] are performed on 150×300 mm ($6'' \times 12''$) cylinders. Unconfined compression tests not only yield a material's uniaxial compressive strength but also provide insight into the damage behavior already starting before the peak-load.

In the present investigation twelve 75×150 mm cylinders each were tested after 31 days and after 400 days, in the middle of the 3-point-bending size-effect investigation. Additionally, eight 150 mm cubes were cut out of the undamaged parts of the ASTM modulus of rupture specimens and fourteen 40 mm cubes were cut from the remainders of the 3-point-bending size effect investigation. The tests were performed

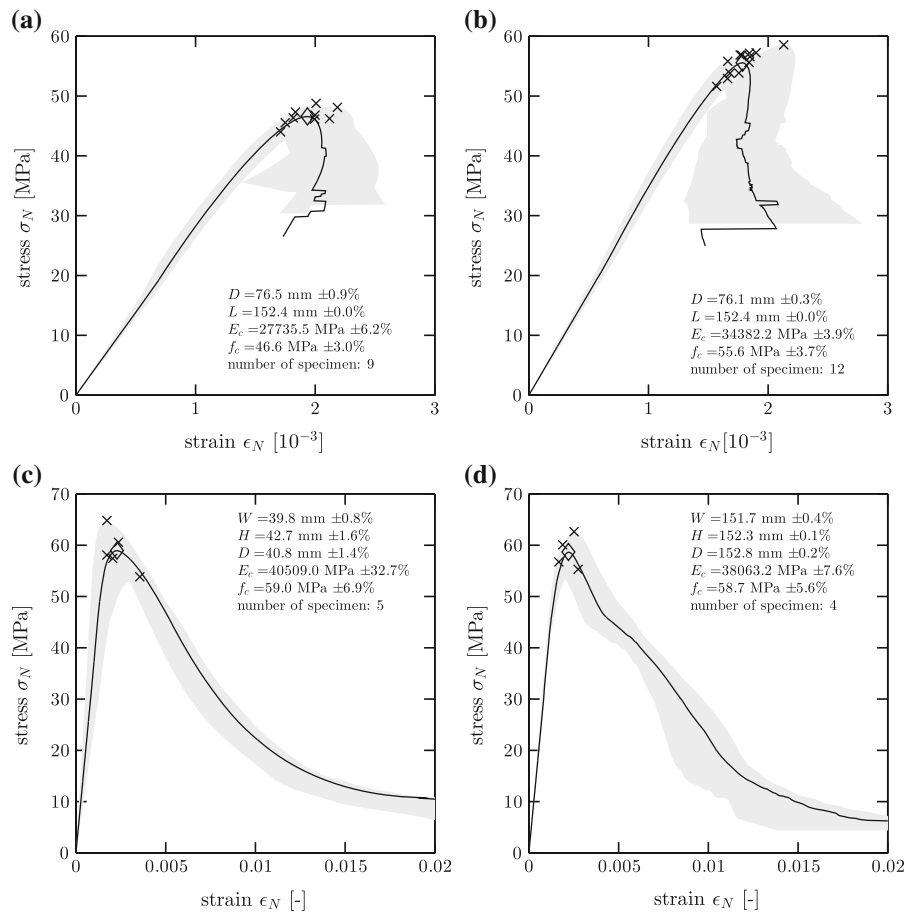


Fig. 4 Nominal stress σ_N versus nominal strain ϵ_N for uniaxial compression tests: **a** cylinder 75 × 150 mm at 31 days, **b** cylinder 75 × 150 mm at 400 days, **c** cubes 40 × 40 mm at 470 days, and **d** cubes 150 × 150 mm at 470 days

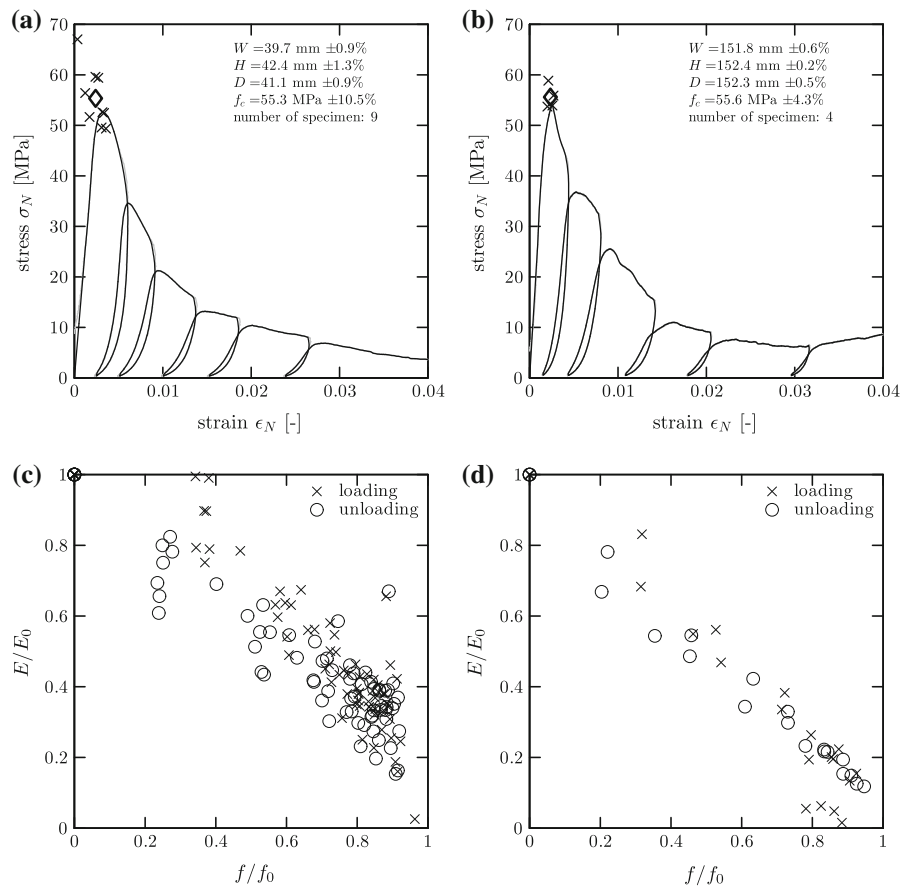
approximately at an age of 470 days in parallel with the Brazilian splitting size effect investigation. During loading only the top load platen was allowed to rotate, in agreement with the ASTM testing standard [65]. All cylinders and the 40 mm cubes were capped with a sulfur compound to ensure initially co-planar and smooth loading surfaces. The 150 mm cubes were loaded on two of the uncut faces that had been cast against the mold. The observed fracture patterns conformed to Type 1 according to ASTM C39 [65] with reasonably well formed cones on both ends. Similarly, pyramid-shaped cones were observed in the cube tests.

It is important to note that friction between specimen and loading platens significantly influences the obtained peak loads by introducing some degree of lateral confinement in the contact surfaces. While this situation can be mimicked in numerical analyses by

suitable boundary conditions, standard analyses assuming ideal uniaxial conditions are thwarted. Typically, this effect is mitigated through the use of friction reducing coatings on the steel platens, teflon sheets, or elastomeric pads. Unfortunately, this practice is limited to normal strength concretes as the compressive strength of modern ultra high performance (UHPC) concretes exceeds the strength of typical friction reducing materials. In case of this investigation solely sulfur compound capping was applied.

The recorded specimen dimensions for cubes comprise the length of all edges as well as the height before and after capping. During testing in addition to force F (recorded by a 450 kN load cell) and machine stroke δ the platen to platen distance u was measured by four equiangularly distributed LVDTs of ± 2.5 mm travel, see Fig. 1d. The chosen stable mode of control was machine stroke.

Fig. 5 Uniaxial compression tests with hysteretic loading-unloading cycles: nominal stress σ_N versus nominal strain ϵ_N for selected curves of **a** 40 mm cubes at 470 days, and **b** 150 mm cubes at 470 days; the relative change in modulus is given in **c** for the 40 mm cubes, and in **d** for the 150 mm cubes



In the case of the cylindrical specimens two perpendicular diameters D were recorded for each end in addition to four height measurements L each before and after capping. Similar to the cube tests force F and piston stroke δ were recorded. The test was controlled by circumferential expansion Δp after a pre-load of roughly 50 % of peak was applied. The axial shortening of the specimen was measured by four equiangularly distributed LVDTs held in place by two symmetric rings with a nominal spacing $g = 100$ mm, see Fig. 1f. Nominal stress σ_N and nominal strain ϵ_N are defined in Eqs. (7) and (8) where \bar{u} = mean shortening of the specimen, \bar{D} is the mean of the specimen dimensions in the respective axis, obtained from four measurements.

$$\sigma_N = \kappa F / \bar{D}^2, \quad \kappa \begin{cases} 1.0 & \text{cube} \\ 4/\pi & \text{cylinder} \end{cases} \quad (7)$$

$$\epsilon_N = \begin{cases} \bar{u} / \bar{D} & \text{cube} \\ \bar{u} / g & \text{cylinder} \end{cases} \quad (8)$$

In Fig. 4 the nominal stress σ_N versus nominal strain ϵ_N diagrams for uniaxial compression tests of 40 mm cubes, 150 mm cubes and 75 × 150 mm cylinders are shown in terms of mean response curves and envelope. Specimen dimensions, peak stresses and elastic moduli are given by mean values and coefficients of variation. Figure 4a, b shows nominal strain as derived from on-specimen measurements while the strain values plotted in Fig. 4c, d are derived from platen to platen measurements and include a compliance correction according to Eq. (6).

For many practical applications (e.g. the analysis of pre-damaged structural members in particular under cyclic loading) also the unloading-reloading behavior in the softening regime is of interest. Fig. 5 provides insight into the damage evolution of unconfined compression tests. Figure 5a, b exemplarily show the nominal stress–strain curves of single cube specimens under hysteretic loading conditions while Fig. 5c, d present the evolution of relative loading and unloading



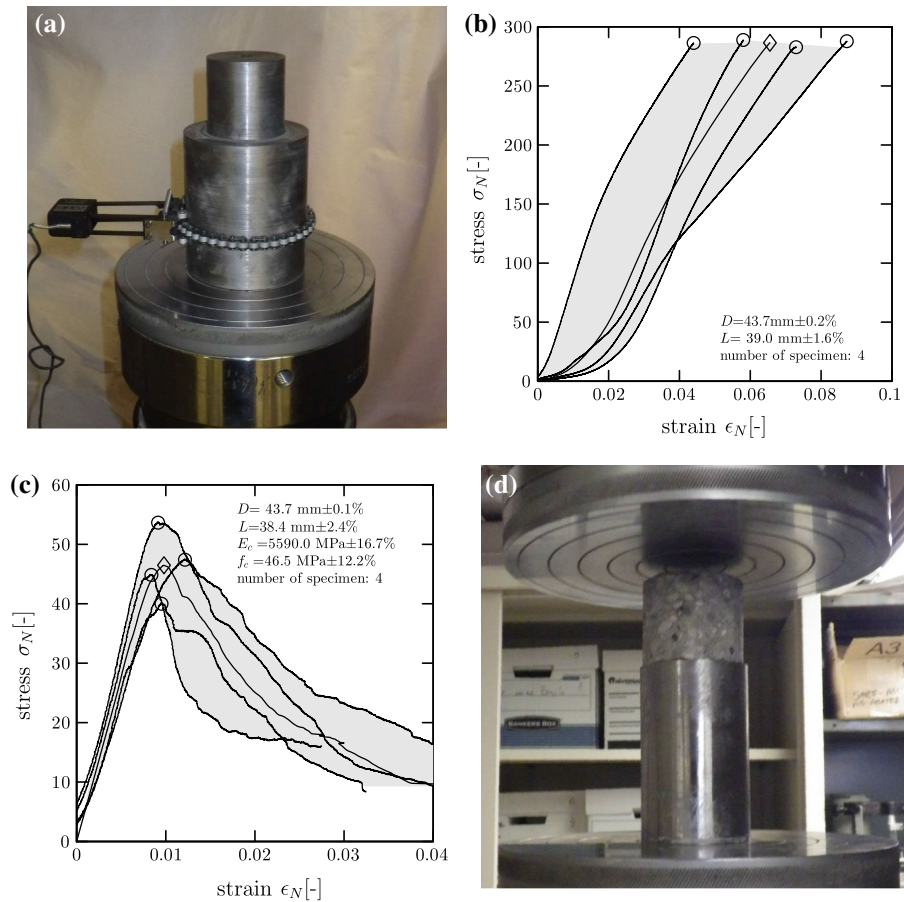


Fig. 6 Compression test under strong passive confinement; **a** test setup for confined test, **b** response under confinement, **c** unconfined response of partner specimen, and **d** setup for unconfined companion specimens

Table 4 Nominal geometry of 3-point-bending specimens

Property	A (mm)	B (mm)	C (mm)	D (mm)
Thickness, W	40.0	40.0	40.0	40.0
Height, D	500	215	92.8	40.0
Length, L	1,200	517	223	96.0
Span, l	1,088	469	202	87.0
Gauge length, g	162;218	94.5;137	60.0;25.4	25.4
Gauge length, g ($\alpha = 0.3$)	25.4	25.4	12.7	12.7
Loading block width, w	60.0	26.0	11.0	5.2
Loading block height, h	40.0	20.0	10.0	5.0

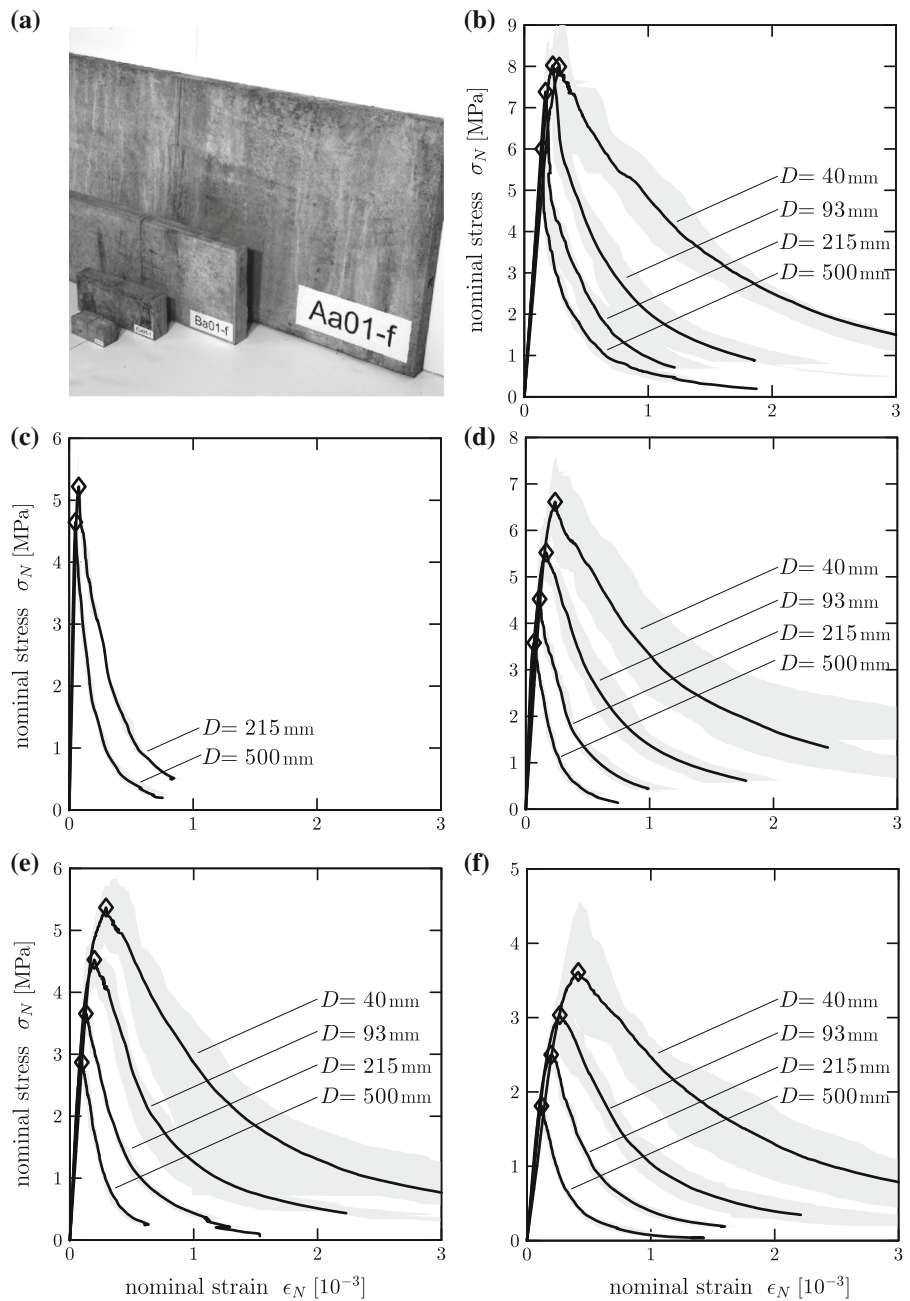
moduli E/E_0 plotted against the relative stress level at the point of unloading f/f_0 . E_0 is the initial loading modulus and f_0 is the peak stress value. The loading

and unloading slopes are obtained through linear regression in the ranges $0.40f < \sigma < 0.80f$ and $0.05f < \sigma < 0.80f$, respectively. The modulus decrease shows a high linear correlation with the decrease in residual strength. Also, the unloading modulus is systematically lower than the reloading modulus.

3.5 Confined compression

In addition to uniaxial unconfined compression ideally also triaxial and hydrostatic test data should be available for calibration. Unfortunately, it was not possible to perform this type of test within the scope of the presented investigation. The closest alternative data source that could be obtained are passively confined compression tests conducted on cored cylinders. High passive confinement was achieved using

Fig. 7 Three point bending: **a** size comparison, **b** nominal stress–strain diagram for un-notched beams, **c** for beams with $\alpha = 2.5\%$, **d** $\alpha = 7.5\%$, **e** $\alpha = 15\%$, and **f** $\alpha = 30\%$



thick-walled steel jackets, see Fig. 6a. In total four confined and four unconfined but otherwise identical specimens were tested. The documented specimen diameter and height are $D = 43.7 \text{ mm} \pm 0.1\%$ and $L = 38.4 \text{ mm} \pm 2.4\%$, respectively. The steel jacket is 88.6 mm high, has an inner diameter of 47.3 mm and a wall thickness of 14.15 mm. The plunger and the bottom loading block provide a very tight fit with a

diameter of 47 mm. For the confined tests the cylinders were grouted into the steel jacket with quickcrete, resulting in a capped height of $L = 41.4 \text{ mm} \pm 2.8\%$. The unconfined partner specimens were not capped. In addition to force F and piston stroke u also the circumferential expansion Δp of the steel jacket as indicator for the confinement was recorded.

Fig. 8 Crack pattern for un-notched beams of **a** size
 $D = 40$ mm, **b** size
 $D = 93$ mm, **c** size
 $D = 215$ mm, **d** size
 $D = 500$ mm

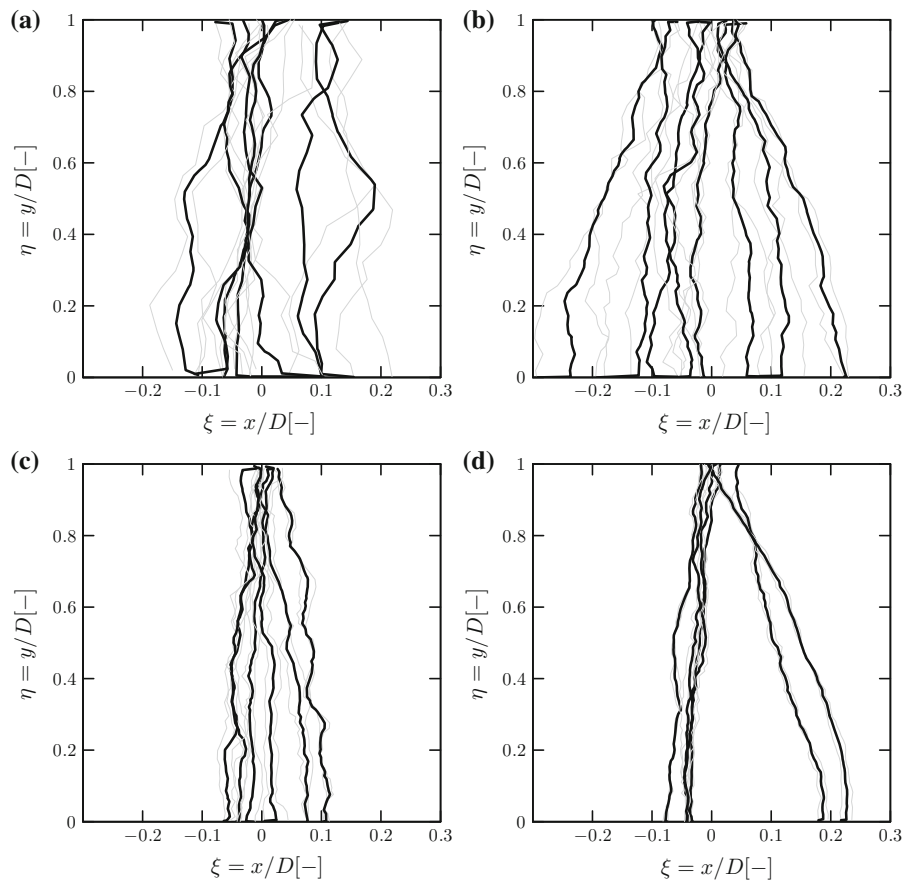


Figure 6b shows the nominal stress strain diagram for the unconfined tests utilizing the definition as introduced in Eqs. (7) and (8), while Fig. 6c presents the response of the unconfined companion specimens (without steel jacket) with otherwise identical setup to maintain the compliance contribution of the setup, see Fig. 6d.

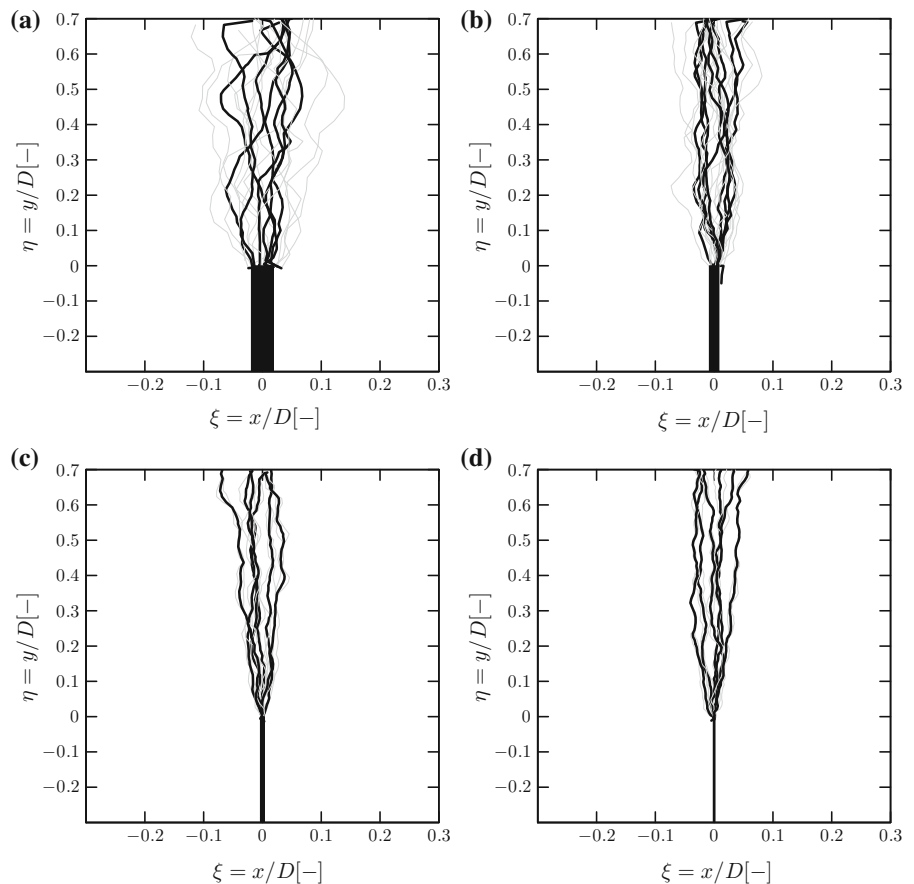
Nominal strain is derived from stroke measurements without correction for the compliance of the test setup. Compared to other uniaxial compression tests, the unconfined cored cylinders show a slight decrease in compressive strength. The response under strong confinement is strongly biased by the grouting material and friction, thus reducing the value of this data.

3.6 Flexural fracture by 3-point-bending

A major part of the presented investigation concerns the characterization of flexural fracture. In particular, the size dependency of flexural strength and toughness are of interest. Further studied parameters include the

relative notch depth $\alpha = a/D$, relative load eccentricity $\xi = x/l$, and the modulus reduction in the softening regime. In total 128 geometrically scaled beams of four sizes with a size range of 1:12.5 were tested. In addition to un-notched specimens, notch depths of $\alpha = 0.3, 0.15, 0.075$ for all sizes and $\alpha = 0.025$ for the two larger sizes were investigated, see also [53]. For each size and notch depth combination at least six specimens were tested, more for the smallest two sizes due to the larger inherent scatter. The specimen geometry is sketched in Fig. 1a and given in Table 4. Except notch width and specimen thickness W all dimensions including the steel support blocks were geometrically scaled. At an age of 96 days the notches were cut with a diamond coated band saw. A lot of attention was placed on minimizing the time that the specimens spent out of the 100 % relative humidity room. The resulting notch width is 1.8 mm. Microscopy revealed a notch-tip geometry that can be well approximated by a half circle with diameter $2r = 1.8$ mm, see Fig. 2b. An even better approximation is obtained with an

Fig. 9 Crack pattern for beams of notch-depth $\alpha = 0.30$ of **a** size $D = 40$ mm, **b** size $D = 93$ mm, **c** size $D = 215$ mm, **d** size $D = 500$ mm



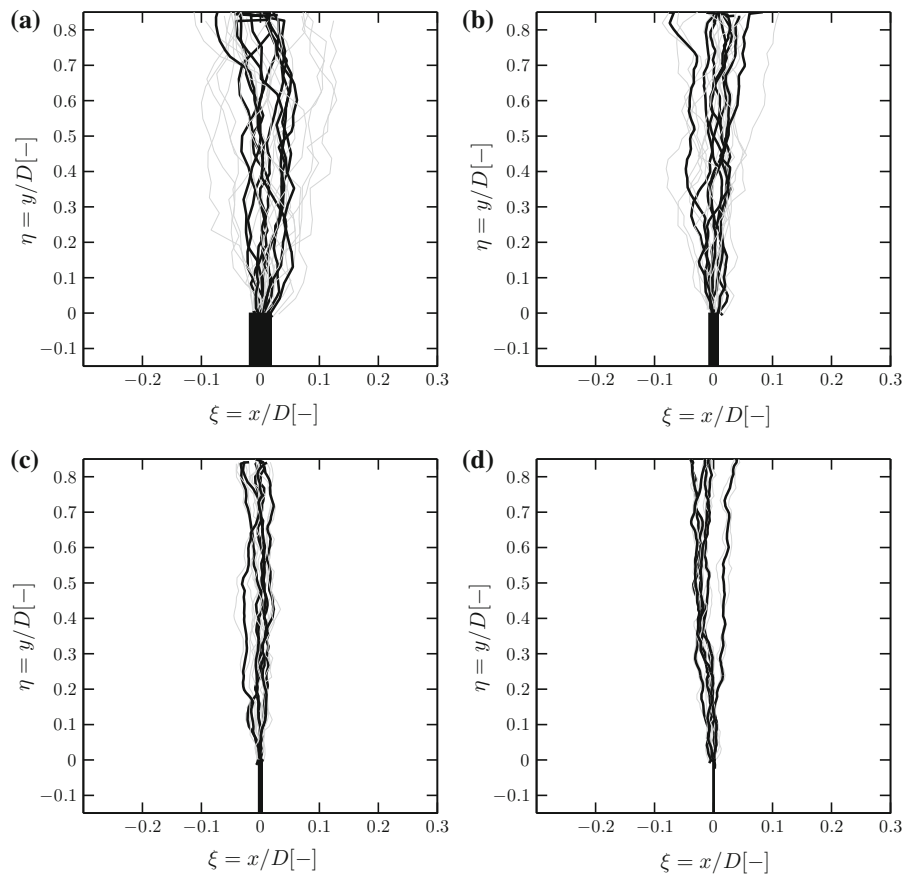
ellipse of transverse diameter $2a = 1.8$ mm and a conjugate diameter $2b = 1.3$ mm. In addition to the geometrically scaled beams a total of 12 standard ASTM modulus of rupture tests [55] were performed in stroke control. The average dimensions according to Fig. 1a are $D = 152.6 \text{ mm} \pm 0.4 \%$ $W = 152.9 \text{ mm} \pm 0.3 \%$ with a nominal length of $L = 558.8$ mm and a span of $l = 457.2$ mm. The loading rate was chosen in such a way that the notch tip would be strained at roughly the same rate for all specimens, corresponding to a loading time of roughly 5 min to peak. For stability reasons the control method was switched from stroke to crack mouth opening at about 60 % of the predicted peak.

Approximately 400 days after casting all 128 beams of the bending size effect investigation were tested within a span of 11 days. The chosen stable mode of control was CMOD for notched specimens and average tensile strain for un-notched beams. Specimens of sizes C and D were loaded in a 90 kN load

frame whereas the larger specimens of sizes A and B were tested in the 1,000 kN load frame. Figure 7a gives a visual overview of the set of beams. Before testing the initial dimensions of all specimens were recorded rigorously and the steel loading blocks glued onto the top and bottom surfaces. Available sensor information included for all tests, in addition to machine force and stroke, center-point displacement, obtained by averaging two LVDT measurements against the load bed, and extensometer readings on the tension side of the beam. The latter correspond to CMOD measurements for the deeper notch depths where the elastic deformation within the gauge length g given in Table 4 is negligible. Specimens with shallower notches and especially un-notched specimens were instrumented with sensors of larger gauge length g to ensure a crack localization within.

The specimen response is plotted in terms of nominal stress σ_N versus nominal strain ϵ_N for the un-notched specimens of all four sizes in Fig. 7b. The

Fig. 10 Crack pattern for beams of notch-depth $\alpha = 0.15$ of **a** size $D = 40$ mm, **b** size $D = 93$ mm, **c** size $D = 215$ mm, **d** size $D = 500$ mm



corresponding plots of notched specimens with relative notch lengths of $\alpha = 0.025, 0.075, 0.15, 0.3$ are given in Fig. 7c–f. For the purpose of this investigation nominal stress σ_N for bending specimens is defined according to beam theory by Eq. (9) where both \bar{D} and \bar{W} are obtained as mean value of 3 and 5–9 measurements at the ligament, respectively. The nominal strain, ϵ_N , definitions are based on the measured opening u of the extensometer with gauge length g and are given in Eq. (10). For specimens with deep notch the crack mouth opening can be fairly well approximated by the extensometer reading at the surface of the beam which is proportional to the CMOD and which is only slightly distorted by elastic deformations in the basically stress free concrete next to the cut. The larger the specimen the closer the extensometer feet can be set to the notch and the smaller this influence becomes. For shorter notches (and especially small specimen) elastic deformations within the gauge length gain in importance but remain

small compared to the total extensometer reading u . Furthermore, these elastic deformations scale if the gauge length scales with specimen size as approximately true in this investigation. Thus, they do not influence size effect investigations and can be neglected in the definition of nominal strain for notched specimens. However, for the sake of accuracy the gauge length (and consequently the contributions of elastic deformations) should be modelled in numerical simulations if model calibration or inverse analysis are to be performed.

For un-notched specimens an engineering strain definition is chosen. In this case, since the gauge length is finite and not negligible compared to span length l a correction factor β is required in order to account for the linear moment distribution in between the extensometer feet with spacing g by converting the average measured strain to peak strain in mid-span. This is especially important since the gauge lengths did not scale with size for this set of tests.

$$\sigma_N = \frac{6F(1 - \xi)\xi l}{\bar{W}D^2} \quad (9)$$

$$\epsilon_N = \begin{cases} \beta u/g & \text{for } \alpha = 0 \\ u/D & \text{for } \alpha > 0 \end{cases} \quad (10)$$

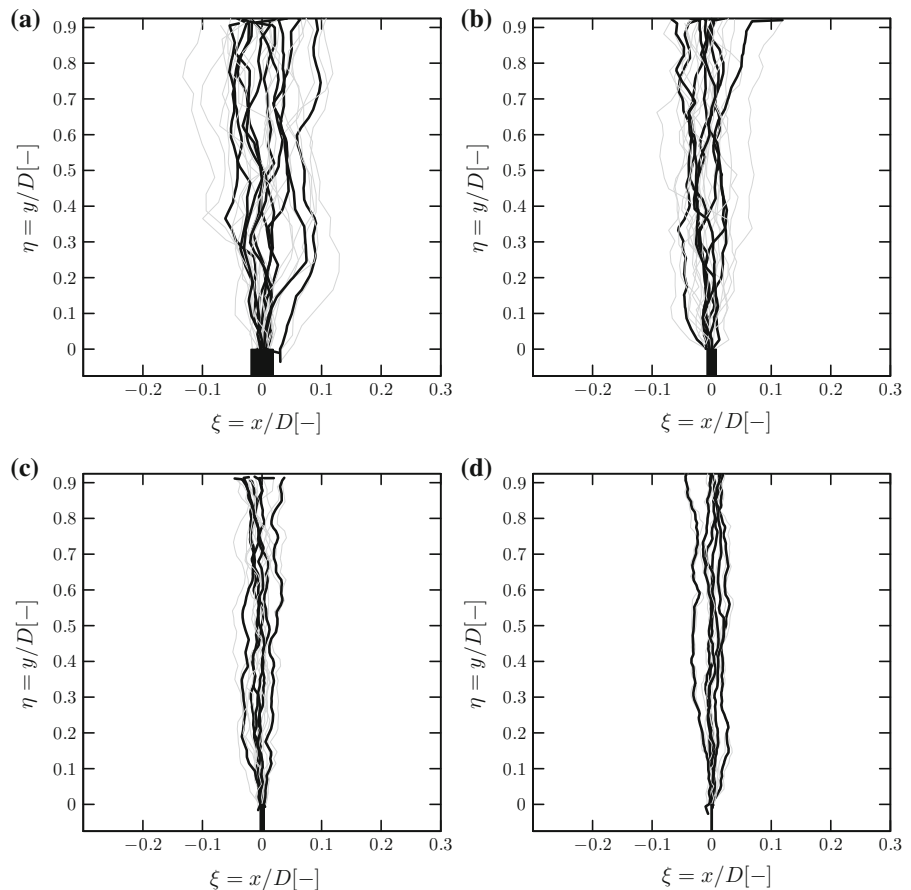
As expected, for increasing specimen size D , strength decreases and the post-peak regime shows a transition from ductile to rather brittle behavior. For all five geometrically similar beam sets the slope in the elastic regime coincides. The traditional presentation of the size effect in flexural strength in the form of a $\log(\sigma_{N,peak})$ versus $\log(D)$ plot is omitted here for the sake of brevity and can be found, together with an extensive analysis and discussion, in Hoover et al. [53, 60, 66].

Concrete is a highly heterogenous material. As such, a significant scatter in structural response due to the random distribution of strength is expected. The macroscopic strength of specimens without initial

notch is influenced most by the material heterogeneity which manifests itself in a wide-spread crack localization on the tension side, see the photogrammetrically obtained crack path distribution of all un-notched specimens in Fig. 8. This variability of local strength is also the cause of statistical distribution of strength, which is, for small material elements, Gaussian with a remote power law tail that gives rise to Weibull distribution [67] when the structure is very large and fails at fracture initiation [68, 69]. In comparison, Figs. 9, 10, 11 and 12 show the crack distributions of the notched beams with all cracks emanating from the notch tip. The grey lines represent the crack path on each surface, while the solid black lines denote the average crack path $x(y)$ over the ligament depth y in a x - y coordinate system, with origin at the crack tip or at the centerpoint on the tension surface, respectively.

Data about the bending shear interaction are available in the form of eccentrically loaded un-

Fig. 11 Crack pattern for beams of notch-depth $\alpha = 0.075$ of **a** size $D = 40$ mm, **b** size $D = 93$ mm, **c** size $D = 215$ mm, **d** size $D = 500$ mm



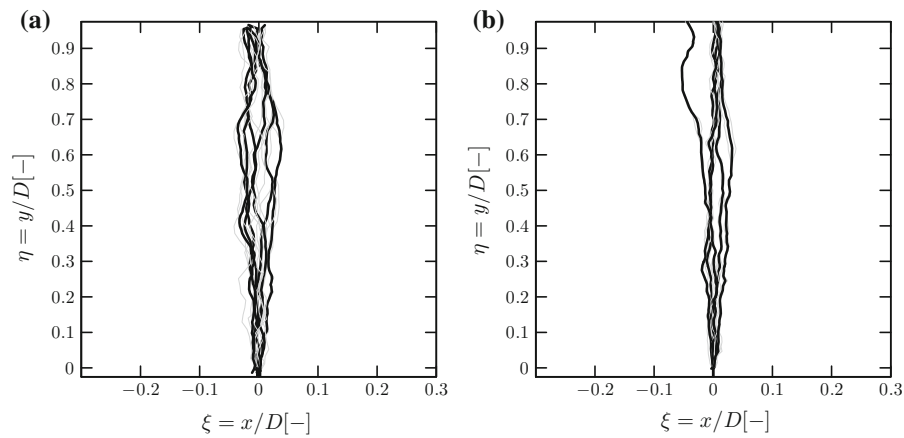
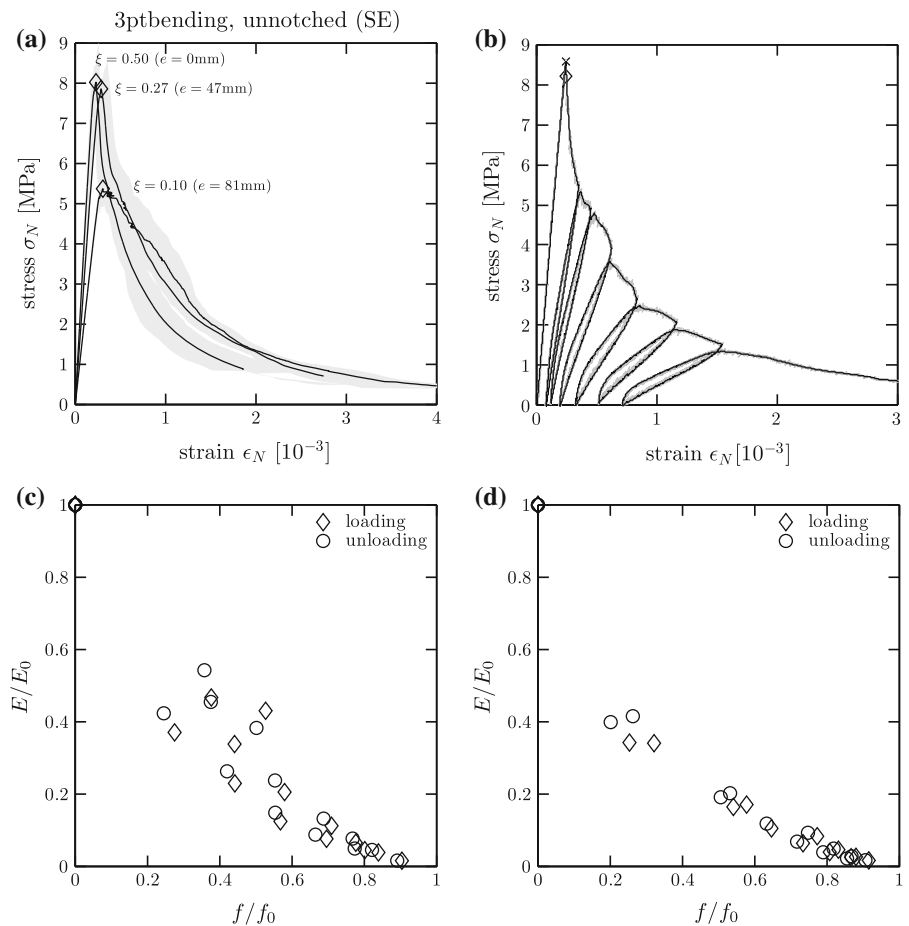


Fig. 12 Crack pattern for beams of notch-depth $\alpha = 0.025$ of **a** size $D = 215$ mm, **b** size $D = 500$ mm

Fig. 13 Three point bending of specimens with $D = 93$ mm: **a** nominal stress strain plot of un-notched beams dependent on eccentricity; **b** example of hysteretically loaded un-notched beam; relative modulus versus relative stress of **c** un-notched beams, and **d** beams with $\alpha = 0.3$



notched beams of the second smallest size with depth $D = 93$ mm. Figure 13a shows nominal stress strain curves for load eccentricities of 47 and 81 mm

corresponding to $\xi = x/l = 0.53, 0.20$ tested at an age of 466 days in comparison with the original centrally loaded beams. Figure 13b presents an

example of an un-notched beam of the same size with loading-unloading cycles in the softening regime. Figure 13c, d finally shows the modulus reduction with softening damage of hysteretically loaded beams of size $D = 93$ mm. The analysis is based on the concept presented in Sect. 3.4. All additional specimens were instrumented with an extensometer of gauge length $g = 44.4$ mm.

3.7 Brazilian splitting tests

The so-called Brazilian splitting test represents another commonly used form of indirect tensions tests in which the specimen is loaded in compression, leading to tensile stresses and ultimately tensile failure in the direction orthogonal to the applied load. The ASTM standard C496 [70] recommends testing cylinders radially under point loads. The specimens are supported and loaded by wooden bearing strips of pre-determined dimensions. While this practice improves the stability of the tests and avoids local failure due to stress singularities, the boundary conditions become ambiguous. Contrarily, the European code EN12390-6 [71] demands direct loading of cylinders by loading blocks, or prisms by loading cylinders. In both cases the curvature ratio is maintained, thus ensuring well defined and equivalent boundary conditions. In the idealized case of elastic response under a concentrated load ($\beta = 0$) the theoretically maximum tensile stress is given by

$$\sigma_{\max}(\beta = 0) = \frac{2F}{\pi WD} \tag{11}$$

If the material were perfectly brittle this equation would give the tensile strength f_t . However, since concrete is a quasi-brittle material this value does not coincide with the true tensile strength but is expected

to be close [72]. It is thus defined as splitting tensile strength f_{st} .

In reality the contact area between support and specimen is always finite with a relative bearing width $\beta = w/D$. Furthermore, standards recommend the use of bearing strips ($0.04 \leq \beta \leq 0.16$) to distribute the loads and avoid local crushing. This distribution of loading leads, for the same total load, to a more uniform stress state in the center of the specimen parallel to the direction of loading and, in consequence, to a reduction in principal tensile stress in the perpendicular direction. This results in a tensile strength increase for increasing bearing strip width and is captured by the correction term $\kappa(\beta)$ that was deduced by Tang for cylindrical specimens [73]. For square prismatic specimens Rocco et al. [72, 74] obtained an empirical equation valid for $\beta < 0.20$.

$$\sigma_{\max}(\beta) = \kappa(\beta) \frac{2F}{\pi WD},$$

$$\kappa(\beta) = \begin{cases} (1 - \beta^2)^{3/2} & \text{for cylinder} \\ (1 - \beta^2)^{5/3} - 0.0115 & \text{for prisms} \end{cases} \tag{12}$$

Table 6 Splitting tensile strength according to size

Label	Specimen size (mm)	Wood (MPa)	Steel (MPa)	Number of specimens (wood/steel)
A	500	4.5 ± 4.5 %	5.2	(5/2)
B	215	5.1 ± 6.0 %	4.9	(5/1)
C	93	5.1 ± 2.5 %	4.9	(7/–)
D	40	5.2 ± 6.3 %	5.0	(9/2)
E	30	5.1 ± 14.9 %	4.5	(7/2)

Table 5 Geometry of Brazilian splitting test specimens

Property	A (mm)	B (mm)	C (mm)	D (mm)	E (mm)
Thickness, W	40.0	40.0	40.0	40.0	40.0
Height, width, D	500	215	92.8	40.0	30.0
Gauge length, g	34.0	34.0	26.0	16.0	8.0
Steel bearing strip width, w	60.0	26.0	11.0	5.2	5.2
Steel bearing strip height, h	40.0	20.0	10.0	5.0	5.0
Wood, initial w	37.6	16.7	7.6	2.7	2.6
wood, initial h	18.4	8.0	3.5	2.7	1.7
wood, final w	46.3	20.1	9.4	4.8	3.5
wood, final h	9.4	4.2	1.9	1.2	1.0



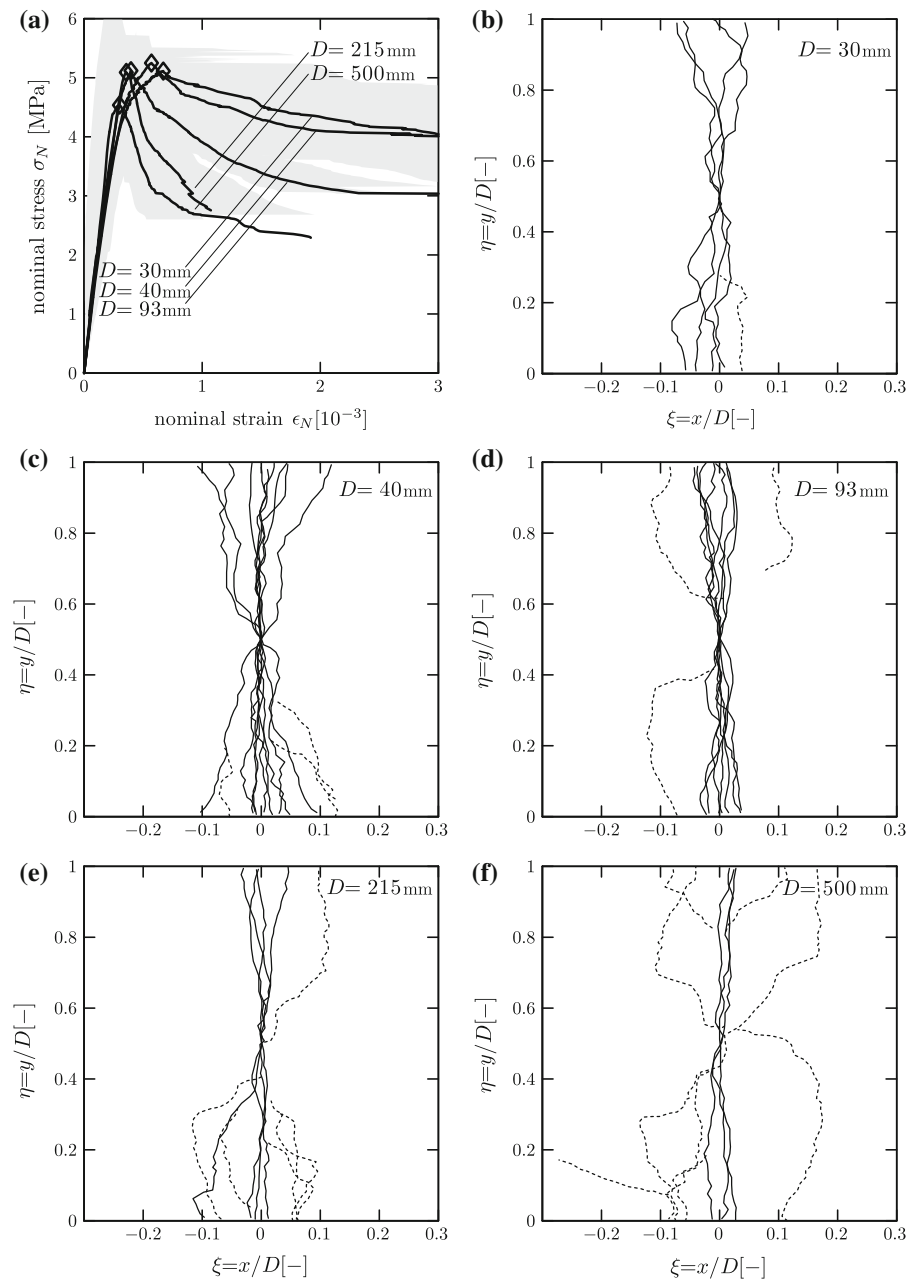


Fig. 14 Brazilian splitting tests; **a** mean nominal stress strain curves and envelopes of specimens with $D = 500, 215, 93, 40, 30$ mm; crack pattern for **b** $D = 30$ mm, **c** $D = 40$ mm, **d** $D = 93$ mm, **e** $D = 215$ mm, and **f** $D = 500$ mm

Within this investigation prismatic specimens according to Fig. 1b of five sizes with constant thickness $W = 40$ mm were tested. In addition to the sizes $D = 40, 93, 215, 500$ of the 3-point-bending tests, specimens of size $D = 30$ were tested, increasing the size range to 1:16.7. Two versions of bearing strips with a relative bearing strip width $\beta \approx 0.08$ were compared -

oak wood and steel. While an average of 6 specimens were tested for each size and wood bearing strips, only 1-2 specimens with steel supports were tested as reference. Unlike the bearing strip width the CMOD gauge length could not be geometrically scaled due to the limited sensor availability. The nominal specimen dimensions, bearing strip width and gauge lengths are



given in Table 5. In the case of oak wood bearing strips the actual average dimensions before and after the tests are given as well.

The specimen response is plotted in terms of nominal stress σ_N versus nominal strain ϵ_N for all five sizes and wooden bearing strips in Fig. 14a. For the purpose of this investigation nominal stress σ_N is defined as maximum tensile stress $\sigma_{\max}(\beta)$ according to Rocco et al. [72, 74] and Eq. (12). Nominal strain is defined as engineering strain utilizing the extensometer opening u and the gauge length g :

$$\epsilon_N = u/g \quad (13)$$

As expected, the nominal stress σ_N decreases with size D and the post-peak response shows a transition from highly ductile to a rather brittle behavior. The nominal strength values of all sizes for both bearing strip versions are reported in Table 6 in terms of mean value and coefficient of variation. In all cases the final, not the initial, width of the bearing strip was used in the determination of nominal stresses. The observed

Table 7 Specimen geometry

Property	Mean (mm)
Thickness, W	$25.6 \pm 1.1\%$
Height, D	$26.4 \pm 2.5\%$
Length, L	$127.4 \pm 0.4\%$
Free length, l	$74.5 \pm 3.5\%$
Notch depth, a	$6.4 \pm 7.8\%$
Gauge length, g	$18.9 \pm 1.1\%$

normalized crack patterns for all specimens with wooden bearing strips are given in Fig. 14b–f according to size. It must be observed that the origin of the coordinate system was chosen in the center of the prism where the highest tensile stresses are to be expected, lacking a better reference point that can be identified on all specimens. Thus, all main cracks (bold lines) seemingly emanate from this point. The secondary cracks that likely formed after the specimen already failed have been recorded relative to the main crack and are presented as dashed lines.

For the analysis only specimens with a stable opening after crack initiation were considered, thus plotted in Fig. 14a, and included in the statistics of Table 6. Contrary to earlier analyses e.g. by Bažant et al. [75] a size-effect is observed but has to be characterized as very mild. Direct loading without wooden bearing strips resulted in a generally lower tensile strength, in spite of the compensation for the bearing strip width. The largest specimen size showed an increase in splitting strength. However, due to the low number of specimens, at best qualitative conclusions can be drawn.

3.8 Torsion

Pure torsion test data were obtained for three cross-sections of width $W = 40$ mm and depth $H = 40, 60, 80$ mm. The specimens were loaded by two opposing moment couples with eccentricity $2e = 20$ mm as sketched in Fig. 1e. Free rotation of all four loading and support points was guaranteed by

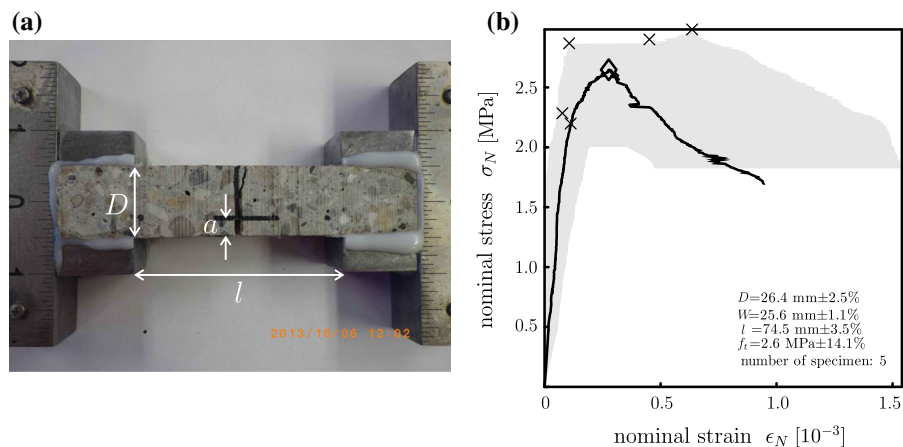


Fig. 15 Single notch tension tests; **a** image of setup; **b** nominal stress σ_N , nominal strain ϵ_N diagram

ball bearings. The span length l was chosen to be 160 mm for the square cross-section and 240 mm otherwise.

The average torsional capacity of the smallest cross-section is $T_{\max} = 52.7 \pm 0.3\%$ Nm. An increase of the cross-sectional depth to $H = 60$ and $H = 80$ mm resulted in an increase of load carrying capacity to $T_{\max} = 84.3 \pm 3.1\%$ Nm and $T_{\max} = 110 \pm 0.2\%$ Nm, respectively. The cracking angle on the initiation face of specimens with rectangular cross-section was determined to be 54.7° for the 80×40 and 49.3° for the 60×40 cross-section. The cracking angle on the opposite faces was measured to be 37.0° and 30.0° , respectively.

Nominal stress may be defined according to the elastic solution for torsion of rectangular cross sections as shear stress τ , based on the mean values of eccentricity \bar{e} , width \bar{W} , and depth \bar{D} , and the torsional moment of inertia J_T . The influence of the aspect ratio D/W is captured by the dimensionless correction factor $\beta = \beta(D/W)$ ($\beta = 0.208$ for $D/W = 1$, $\beta = 0.231$ for $D/W = 1.5$, and $\beta = 0.246$ for $D/W = 2$).

$$\sigma_N = \tau = \frac{M_T r}{J_T} = \frac{F \bar{e}}{\beta \bar{W}^2 \bar{D}} \quad (14)$$

The corresponding nominal strain is defined based on the rate of the angle of twist ϑ' by

$$\epsilon_N = \vartheta' r = \frac{\delta \bar{D}}{\bar{e} \cdot l/2} \quad (15)$$

where δ = measured load point displacement.

3.9 Direct tension tests

Single notch direct tension tests on approximately 950 day old concrete prisms, cut from undamaged pieces of the original size effect investigation, were performed. The specimen dimensions are given in Table 7. In order to ensure localization of the crack in the center cross-section and thus be able to control the test by crack mouth opening a notch with a relative depth $\alpha = a/D = 0.25$ was cut, see Fig. 15a. The boundary conditions are characterized by fully clamped support on one side and pin support on the other end as sketched in Fig. 1g.

The nominal stress is defined according to the elastic solution of un-notched specimens according to

Eq. (16) while nominal strain is defined as engineering strain based on the measured extensometer opening u . The resulting nominal stress–strain diagram is given in Fig. 15 with one removed outlier.

$$\sigma_N = \frac{F}{WD} \quad (16)$$

$$\epsilon_N = u/g \quad (17)$$

4 Conclusion and outlook

A comprehensive data-set consisting of 152 notched and un-notched beams, 32 cylinders, 28 cubes, 46 Brazilian splitting prisms, 6 single notch tension tests, and 11 torsion tests has been presented. Post-peak data and failure mode in terms of crack patterns are available for almost every specimen tested. With a size range of 1:12.5 for the bending investigation and 1:16.7 for the splitting tests, this data-set contains some of the largest size-effect investigations on plain concrete, and thus represents an ideal data source for model development and calibration which can be found at '<http://www.baunat.boku.ac.at/cd-labor/downloads/versuchsdaten>'.

Acknowledgments The financial support by the Austrian Federal Ministry of Economy, Family and Youth and the National Foundation for Research, Technology and Development for part of the analysis is gratefully acknowledged, as is the financial support from the U.S. Department of Transportation, provided through Grant No. 20778 from the Infrastructure Technology Institute of Northwestern University, for the initial size effect investigation. The work of G. Cusatis was supported under NSF Grant No. 0928448.

References

1. Wille K, Naaman AE, El-Tawil S, Parra-Montesinos GJ (2012) Ultra-high performance concrete and fiber reinforced concrete: achieving strength and ductility without heat curing. *Mater Struct* 45:309–324
2. Naik TR, Kumar R, Ramme BW, Canpolat F (2012) Development of high-strength, economical self-consolidating concrete. *Constr Build Mater* 30:463–469
3. Fantilli AP, Vallini P, Chiaia B (2011) Ductility of fiber-reinforced self-consolidating concrete under multi-axial compression. *Cem Concr Compos* 33(4):520–527
4. Wang H, Belarbi A (2011) Ductility characteristics of fiber-reinforced-concrete beams reinforced with FRP rebars. *Constr Build Mater* 25(5):2391–2401



5. Yang E-H, Li VC (2012) Tailoring engineered cementitious composites for impact resistance. *Cem Concr Res* 42(8):1066–1071
6. Hillerborg A, Mod er M, Petersson PE (1976) Analysis of crack formation and crack growth in concrete by means of fracture mechanics and finite elements. *Cem Concr Res* 6:773–782
7. Hillerborg A (1985) The theoretical basis of a method to determine the fracture energy G_f of concrete. *Mater Struct* 18(4):291–296
8. Ba ant ZP, Planas J (1998) Fracture and size effect in concrete and other quasibrittle materials. CRC Press, Boca Raton
9. Irwin GR (1958) Fracture, vol VI of Encyclopaedia of physics. Springer, Berlin
10. Hilsdorf HK, Lorman WR, Monfore GE (1973) Triaxial testing of nonreinforced concrete specimens. *J Test Eval* 1(4):330–335
11. Ba ant ZP, Bishop FC, Chang TP (1986) Confined compression tests of cement paste and concrete up to 300 Ksi. *ACI J Proc* 83(4):553–560
12. Gabet T, Mal cot Y, Daudeville L (2008) Triaxial behaviour of concrete under high stresses: influence of the loading path on compaction and limit states. *Cem Concr Res* 38(3):403–412
13. Ba ant ZP, Kim JHH, Brocca M (1999) Finite strain tube-squash test of concrete at high pressures and shear angles up to 70 degrees. *ACI Mater J* 96(5):580–592
14. Brocca M, Ba ant ZP (2001) Microplane finite element analysis of tube-squash test of concrete with shear angles up to 70. *Int J Numer Methods Eng* 52(10):1165–1188
15. Jir sek M, Ba ant ZP (2002) Inelastic analysis of structures. Wiley, London
16. Han D-J (2007) Plasticity for structural engineers. J. Ross Publishing, Fort Lauderdale
17. Ba ant ZP, Cedolin L (1991) Stability of structures: elastic, inelastic, fracture and damage theories, 2nd edn. Oxford University Press, New York
18. Bittnar Z,  ejnoha J (1996) Numerical methods in structural mechanics. ASCE Publications, New York
19. Taylor GI (1938) Plastic strain in metals. *J Inst Met* 63:307–324
20. Lin TH (1968) Theory of inelastic structures. Wiley, New York
21. Ba ant ZP, Byung HO (1985) Microplane model for progressive fracture of concrete and rock. *J Eng Mech* 111(4):559–582
22. Cusatis G, Zhou X (2013) High order microplane theory for quasi-brittle materials with multiple characteristic lengths. *J Eng Mech* 140(7):04014046
23. Ba ant ZP, O bolt J (1992) Compression failure of quasi-brittle material: nonlocal microplane model. *J Eng Mech* 118(3):540–556
24. Hasegawa T, Ba ant ZP (1993) Nonlocal microplane concrete model with rate effect and load cycles. I: general formulation. *J Mater Civ Eng* 5(3):372–393
25. Caner FC, Ba ant ZP (2012) Microplane model M7 for plain concrete: I. Formulation. *J Eng Mech* 139(12):1724–1735
26. Di Luzio G, Cusatis G (2013) Solidification-microprestress-microplane (SMM) theory for concrete at early age: theory, validation and application. *Int J Solids Struct* 50(6):957–975
27. Cusatis G, Beghini A, Ba ant ZP (2008) Spectral stiffness microplane model for quasibrittle composite laminates, part I: theory. *J Appl Mech* 75(2):021009–021009-9
28. Beghini A, Cusatis G, Ba ant ZP (2008) Spectral stiffness microplane model for quasibrittle composite laminates, part II: calibration and validation. *J Appl Mech* 75(2):021010–021010
29. de Borst R, Guti rrez MA, Wells GN, Remmers JJC, Askes H (2004) Cohesive-zone models, higher-order continuum theories and reliability methods for computational failure analysis. *Int J Numer Methods Eng* 60(1):289–315
30. Jir sek M (1998) Nonlocal models for damage and fracture: comparison of approaches. *Int J Solids Struct* 35(31–32):4133–4145
31. Ba ant ZP, Jir sek M (2002) Nonlocal integral formulations of plasticity and damage: survey of progress. *J Eng Mech* 128(11):1119–1149
32. Ba ant ZP, Oh BH (1983) Crack band theory for fracture of concrete. *Mater Struct* 16:155–177
33. Needleman A, Tvergaard V (1987) An analysis of ductile rupture modes at a crack tip. *J Mech Phys Solids* 35(2):151–183
34. Mo es N, Dolbow J, Belytschko T (1999) A finite element method for crack growth without remeshing. *Int J Numer Methods Eng* 46(1):131–150
35. Ortiz M, Pandolfi A (1999) Finite-deformation irreversible cohesive elements for three-dimensional crack-propagation analysis. *Int J Numer Methods Eng* 44(9):1267–1282
36. Rocco C, Guinea GV, Planas J, Elices M (2001) Review of the splitting-test standards from a fracture mechanics point of view. *Cem Concr Res* 31(1):73–82
37. Cusatis G, Ba ant ZP, Cedolin L (2003) Confinement-shear lattice model for concrete damage in tension and compression: I. Theory. *J Eng Mech* 129:1439
38. Cusatis G, Ba ant ZP, Cedolin L (2003) Confinement-shear lattice model for concrete damage in tension and compression: II. Computation and validation. *J Eng Mech* 129:1449
39. Cusatis G, Ba ant ZP, Cedolin L (2006) Confinement-shear lattice CSL model for fracture propagation in concrete. *Comput Methods Appl Mech Eng* 195(52):7154–7171
40. Cusatis G (2011) Strain-rate effects on concrete behavior. *Int J Impact Eng* 38(4):162–170
41. Ba ant ZP, Tabbara MR, Kazemi MT, Pijaudier-Cabot G (1990) Random particle model for fracture of aggregate or fiber composites. *J Eng Mech* 116(8):1686–1705
42. Lilliu G, van Mier JGM (2003) 3D lattice type fracture model for concrete. *Eng Fract Mech* 70:927–941
43. Yip M, Li Z, Liao B, Bolander JE (2006) Irregular lattice models of fracture of multiphase particulate materials. *Int J Fract* 140:113–124
44. Gianluca C, Hikaru N (2011) Discrete modeling of concrete materials and structures. *Cem Concr Compos* 33(9):865–866
45. Cusatis G, Mencarelli A, Pelessone D, Baylot J (2011) Lattice discrete particle model (LDPM) for failure behavior of concrete. II: calibration and validation. *Cem Concr Compos* 33(9):891–905
46. Cusatis G, Pelessone D, Mencarelli A (2011) Lattice discrete particle model (LDPM) for failure behavior of concrete. I: theory. *Cem Concr Compos* 33(9):881–890
47. Schaufert EA, Cusatis G (2011) Lattice discrete particle model for fiber-reinforced concrete. I: theory. *J Eng Mech* 138(7):826–833



48. Schaufert EA, Cusatis G, Pelessone D, O'Daniel J, Baylot J (2012) Lattice discrete particle model for fiber-reinforced concrete. II: tensile fracture and multiaxial loading behavior. *J Eng Mech* 138(7):834–841
49. Cusatis G (2013) The lattice discrete particle model (LDPM) for the numerical simulation of concrete behavior subject to penetration. Wiley, London, pp 369–387
50. Alnaggar M, Cusatis G, Di Luzio G (2013) Lattice discrete particle modeling (LDPM) of Alkali Silica reaction (ASR) deterioration of concrete structures. *Cem Concr Compos* 41:45–59
51. Kim KT, Zdeněk P, Bažant P, Yu Q (2013) Non-uniqueness of cohesive-crack stress-separation law of human and bovine bones and remedy by size effect tests. *Int J Fract* 181(1):67–81
52. Caner FC, Bažant ZP, Wendner R (2013) Microplane model M7f for fiber reinforced concrete. *Eng Fract Mech* 105:41–57
53. Hoover CG, Bažant ZP, Vorel J, Wendner R, Hubler MH (2013) Comprehensive concrete fracture tests: description and results. *Eng Fract Mech* 114:92–103
54. Morteza MHA, Kazemi MT, Nikbin IM, Amiri JV (2013) The effect of water to cement ratio on fracture parameters and brittleness of self-compacting concrete. *Mater Des* 50:267–276
55. ASTM (2010) C293: standard test method for flexural strength of concrete (using simple beam with center-point loading)
56. Grubbs FE (1969) Procedures for detecting outlying observations in samples. *Technometrics* 11(1):1–21
57. Stefansky W (1972) Rejecting outliers in factorial designs. *Technometrics* 14(2):469–479
58. Model code 2010—final draft, vol 1. Technical Report, fib, 2012
59. ACI (2008) 209.2R: guide for modeling and calculating shrinkage and creep in hardened concrete. Technical Report
60. Hoover CG, Bažant ZP (2013) Comprehensive concrete fracture tests: size effects of types 1 & 2, crack length effect and postpeak. *Eng Fract Mech* 110:281–289
61. Nakayama J (1965) Direct measurement of fracture energies of brittle heterogeneous materials. *J Am Ceram Soc* 48(11):583–587
62. Tattersall HG, Tappin G (1966) The work of fracture and its measurement in metals, ceramics and other materials. *J Mater Sci* 1(3):296–301
63. Concrete—part 1: specification, performance, production and conformity, 2000
64. Eurocode 2 (2004) Design of concrete structures, part 1–1: general rules and rules for buildings
65. ASTM (2012) C39: standard test method for compressive strength of cylindrical concrete specimens
66. Hoover CG, Bažant ZP (2014) Universal size-shape effect law based on comprehensive concrete fracture tests. *J Eng Mech* 140(3):473–479
67. Weibull W (1939) The phenomenon of rupture in solids, vol 153. Royal Swedish Institute of Engineering Research, Stockholm, pp 1–55
68. Le J-L, Bažant ZP, Bazant MZ (2011) Unified nano-mechanics based probabilistic theory of quasibrittle and brittle structures: I. Strength, static crack growth, lifetime and scaling. *J Mech Phys Solids* 59(7):1291–1321
69. Le J-L, Bažant ZP (2011) Unified nano-mechanics based probabilistic theory of quasibrittle and brittle structures: II. Fatigue crack growth, lifetime and scaling. *J Mech Phys Solids* 59(7):1322–1337
70. ASTM (2011) C496: standard test method for splitting tensile strength of cylindrical concrete specimens
71. CEN (2009) EN12390-6: testing hardened concrete
72. Rocco C, Guinea GV, Planas J, Elices M (1999) Size effect and boundary conditions in the Brazilian test: theoretical analysis. *Mater Struct* 32(6):437–444
73. Tang T (1994) Effects of load-distributed width on split tension of un-notched and notched cylindrical specimens. *J Test Eval* 22(5):401–409
74. Rocco C, Guinea GV, Planas J, Elices M (1999) Size effect and boundary conditions in the Brazilian test: experimental verification. *Mater Struct* 32(3):210–217
75. Bažant ZP, Kazemi MT, Hasegawa T, Mazars J (1991) Size effect in Brazilian split-cylinder tests. Measurements and fracture analysis. *ACI Mater J* 88(3):325–332